# Compression of gaseous hydrogen into warm dense states up to 95 GPa using multishock compression technique

Guo-Jun Li [1,2,3] Yun-Jun Gu,[2,*] Yang-Shun Lan [1,2] Qi-Feng Chen [1,2,4,†] Zhi-Guo Li [2] Lei Liu [4]
Zhao-Qi Wang [5] Zhi-Jun Shen,[6] and Xiang-Rong Chen [1,‡]

[1]*College of Physics, Sichuan University, Chengdu 610065, China*
[2]*National Key Laboratory for Shock Wave and Detonation Physics, Institute of Fluid Physics,*
*Chinese Academy of Engineering Physics, Mianyang 621900, China*
[3]*School of Physics, Henan Normal University, Xinxiang 453007, China*
[4]*School of Science, Southwest University of Science and Technology, Mianyang 621010, China*
[5]*College of Science, Xi'an University of Science and Technology, Xi'an 710054, China*
[6]*Laboratory of Computational Physics, Institute of Applied Physics and Computational Mathematics, Beijing 100088, China*

The thermodynamic properties of warm dense hydrogen, such as the equation of state (EOS) and sound velocity, affect our understanding of the evolution and interior structures of gas giant planets. However, for this low-$Z$ gas, obtaining the EOS and sound velocity experimentally under relevant planetary conditions is challenging because the extremely warm states are difficult to reach, characterize, and interrogate. Here, the multishock compression technique is used to generate the thermodynamic states of warm dense hydrogen. This provides a dynamic loading from shock adiabatic to quasi-isentropic compressions, covering wide pressure and density ranges of 0.02–95 GPa and 0.01–0.64 g/cm$^3$, which enables us to determine the EOS and infer the high-pressure sound velocities of warm dense hydrogen relevant to planetary interiors. The data obtained in this way are comprehensively compared with several important theoretical models for astrophysics applications. The present experiments provide desirable principal- and off-Hugoniot states for revisiting the thermodynamic space of existing experimental data. These observations and thermodynamic states may be important in guiding future theoretical developments and constructing interior structure models for gas giant planets.

## I. INTRODUCTION

Hydrogen is the dominant component of gas giant planets. Thus, accurate knowledge about the equation of state (EOS) and sound velocity of hydrogen is vital in astrophysics applications, as this could provide a bridge between astronomical observations and planetary interiors [1–4]. In addition, hydrogen serves as an excellent prototype for establishing theoretical models due to its simple atomic structure [2]. Various shock-loading experiments for hydrogen and its isotope deuterium, using two-stage light-gas guns [5–8], magnetically launched flyers [9–12], laser-driven shocks [13–20], or convergent explosives [21–25], have motivated the development of numerous theoretical methods, including chemical models [26–28] and first-principles methods [29–35]. The majority of these dynamic experimental measurements have been performed under single- or double-shock compression, and have focused on comparing the measured results for cryogenic liquid deuterium on the principal-Hugoniot curve with those predicted by various theoretical models

[9–13,15–18,20,21]. The maximum shock pressure of deuterium has reached 550 GPa in experiments [20]. Recent high-precision measurements of deuterium loaded by magnetically launched flyers show that most of the theoretical models give unsatisfactory results regarding the onset of dissociation and the maximum compression along the principal-Hugoniot curve [12], presenting a tremendous challenge to construct more accurate theoretical models. Compared to deuterium, shock compression experiments for hydrogen are relatively rare [17,19]. To date, the highest experimental pressure for hydrogen along the principal-Hugoniot curve is much lower than that for deuterium because hydrogen has a lower shock impedance and its high-pressure and high-temperature states are more difficult to reach at the same loading conditions.

Compared with single- or double-shock compression, the multishock compression produced by the reverberating-shock technique can probe a broader range of thermodynamic paths [7,8,23–25,36,37] and is an efficient method for investigating the insulator-metal (IM) transition at high pressures and high temperatures [7,8,36,37]. The conductivity of hydrogen measured by Nellis, Weir, and Mitchell (NWM) in multishock compression experiments shows that the IM transition occurs at ∼140 GPa and ∼3000 K [7,8]. The theoretically predicted plasma phase transition (PPT) [38,39] of deuterium was observed in a multishock compression generated by convergent

explosives [23]. However, the observed signature of the PPT—a density jump—is still to be confirmed theoretically and in further experiments [24,40–42]. Recently, multishock experiments driven by magnetically launched flyers [36] and lasers [37] have been used to probe the IM transition of deuterium, based on changes in the measured optical properties. However, the experimental results for the IM transition from these two approaches have relatively obvious differences, and thus, the experiments provide no definite conclusion [43–45]. Despite the PPT and IM transition having been investigated using the reverberating-shock technique, the determination of multishock compression paths is not entirely clear from the experimental measurements and requires theoretical simulations [7,8,23,24,36,37]. For example, in two-stage light-gas gun experiments [7,8], NWM simply measured the final state of the reverberating-shock compressions, whereas in convergent-explosive experiments [23,24], the recorded pressures stem from the gas-dynamic calculations. Therefore, it is necessary to determine the multishock paths of hydrogen directly from measurements without the help of theoretical simulations. In addition, experimental multishock paths provide a good opportunity to determine the sound velocity of hydrogen, for which experimental results [46] are deficient under high-pressure and high-temperature conditions.

In this study, multishock compression experiments on gaseous $H_2$ were performed to explore its dynamic response properties. Its electrical conductivity was calculated via the first-principles method to analyze the electrical properties corresponding to the multishock states. The shock reverberation process was clearly observed, which ensures a completely experimental determination of the multishock states (except for the temperature) up to 95 GPa. The sound velocity was also derived from the experimental multishock states of hydrogen at ∼65–95 GPa.

## II. EXPERIMENTAL METHODS

The inset of Fig. 1 is a schematic diagram of the experimental configuration for performing the multishock compression. It follows similar successful experiments conducted on He [47] and the $D_2$–He mixture [48]. In the current experiment, ∼6.4–7.2-mm-thick gaseous $H_2$ samples were prepressurized to 20 or 40 MPa at room temperature through the external pressurizing device and sealed in a sample cell, which has a front 304 steel (S304) baseplate and a rear composite window. The composite window consists of a ∼0.13-mm-thick aluminum (Al) film with an aperture with a diameter of ∼4 mm at the center as well as ∼4.0-mm-thick LiF and ∼2.0-mm-thick sapphire ($Al_2O_3$). The specially designed window allows us to simultaneously monitor the light radiation from the compressed gaseous hydrogen and the particle velocity at the hydrogen-window interface. A two-stage light-gas gun with a bore diameter of ∼30 mm was used to accelerate a tantalum (Ta) flyer with a diameter of ∼28 mm and thickness of ∼3.2 mm to a velocity of 4.9–5.6 km/s, as measured by a magnetic velocity induction system with uncertainties 0.5%. A strong shock wave was generated when the Ta flyer impacted the S304 baseplate. The shock wave was transmitted into the hydrogen sample from the baseplate, then propagated and reflected between the baseplate and window
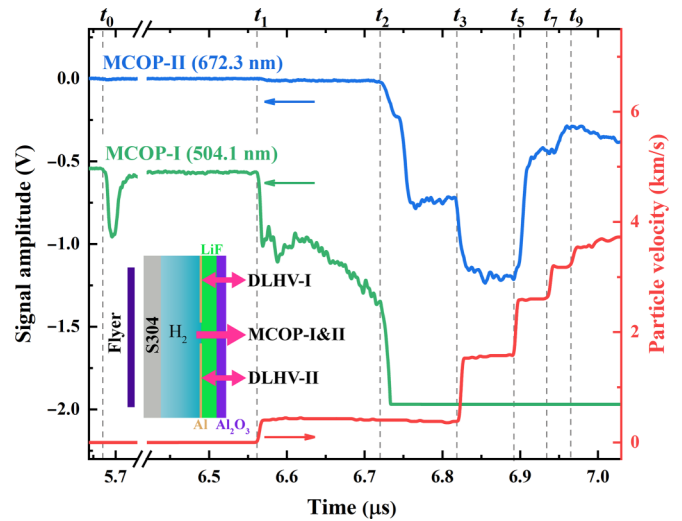


FIG. 1. Representative signals from the MCOP and DLHV instruments for shot no. H18704. The light radiation histories of $H_2$ recorded by the 504-nm-wavelength channel of MCOP-I and 672-nm-wavelength channel of MCOP-II are represented as green and blue lines, respectively. The intensity is indicated by the voltage signal. For clarity, the MCOP-I signal amplitude has been shifted downward by 0.55 V. The red line is the velocity history at the $H_2$-window interface recorded by DLHV-II. Note that the values directly observed by DLHV-II are apparent velocities and have been corrected using the refractive index of lithium fluoride (LiF) [51–53]. $t_0, t_1, t_2, \ldots$ are the shock arrival times at the baseplate-$H_2$ and $H_2$-window interfaces. Inset: Schematic diagram of a target designed for the multishock compression (dimensions are not to scale).

since the shock dependence of the baseplate and window were higher than that of hydrogen. During the multishock compressions, the density, pressure, and temperature in the sample increased, so that it changed from a dense gaseous to a warm dense state. The emissions from the $H_2$ under these shock compressions were recorded using two sets of multichannel optical pyrometers (MCOPs) [49] with different sensitivities, while the velocity history of the $H_2$-window interface was measured via two sets of dual laser heterodyne velocimetries (DLHVs) through the Doppler shift interference fringes of the reflected light [50] (see the inset of Fig. 1).

Typical MCOP and DLHV measurements are shown in Fig. 1 and in Figs. S1 and S7 of the Supplemental Material (SM) [54] for shot no. H18704. The multishock compression process can be distinctly distinguished from these signals. The high-sensitivity MCOP-I signals indicate that the first shock wave entered the hydrogen sample from the baseplate at $t_0$. Note that an intense rise in the signal amplitude occurred at $t_0$, then a peak of narrow time width in the starting stage was formed, and, finally, a stable plateau lasted until $t_1$. Here, the signal amplitudes in the stable plateau were used to determine the first-shock temperature; detailed discussions about the physical meaning of the peak and the first-shock temperature determination can be found in Sec. I of the SM [54]. At $t_1$, the first-shock wave in the sample arrived at the $H_2$-window interface. And a reflected shock wave was generated and compressed the $H_2$ to the second-shock state with a higher temperature, which induced the MCOP signal amplitude to

rise. At the same time, the transmitted shock wave entered the window and compressed the window to the first-shock state, resulting in the first step rise in the DLHV-II signals. At $t_2$, the second-shock wave in the sample arrived at the H$_2$-baseplate interface and was then reflected. The reflected shock wave entered the H$_2$, causing the third shock and the signal amplitude of MCOP-II increased again, implying that the light radiated from the shock wave front of the third shock could still partially penetrate the compressed layer of the H$_2$ under the second-shock state. Note that the light radiated from the third-shock sample is beyond the measurement range of MCOP-I. Similarly, at $t_3$, the third-shock wave arrived at the H$_2$-window interface. The window was shocked to the second-shock state, and the DLHV signals rose again quickly to a higher plateau. Meanwhile, the H$_2$ was compressed to the fourth-shock state, and the MCOP-II signal amplitude strengthened further. For later multishocks, the moments $t_4$, $t_6$, $t_8$ when shock waves arrived at the H$_2$-baseplate interface cannot be observed from the MCOP-II signal, while the moments $t_5$, $t_7$, $t_9$ when shock waves arrived at the H$_2$-window interface can be discriminated in the DLHV signal. The combination of measured $t_1$, $t_3$, $t_5$, ..., and the particle velocity of the hydrogen-window interface measured by the DLHV can be used to determine the $t_4$, $t_6$, $t_8$ based on the wave propagation relation in the multishock compression process and shock wave velocities, pressures, and densities of multishock states using the impedance matching method, whose detailed inferences can be found in Sec. II of the SM [54]. Note that the uncertainties of the LiF and S304 EOS are not taken into account when using the impedance matching method to determine the multishock states of hydrogen beyond the fourth shock. Therefore, the obtained standard uncertainties should be viewed as lower bounds. In addition, the first- and second-shock temperatures were determined by fitting the spectral radiance recorded by the MCOP to the gray Planck model; see Sec. I of the SM [54].

### III. RESULTS AND DISCUSSIONS

Three shots were applied to hydrogen samples, and the multishock EOS data were obtained covering a wide range of pressures (0.02–95 GPa) and densities (0.015–0.64 g/cm$^3$) and spanning a region from a dense gaseous state to a warm dense state (Table S4 of the SM [54]). These data provide adequate information for validating the theoretical models. In Fig. 2 and Fig. S22 of the SM [54], the current data are compared with results from several important theoretical models, including the chemical models SESAME [26], Saumon, Chabrier, and van Horn (SCVH) [27], and self-consistent fluid variational theory (SFVT) [28], and recently developed multiphase EOS models of the Rostock group (REOS.3) [33] and Chabrier, Mazevet, and Soubiran (CMS) [35]. The REOS.3 and CMS models were constructed based on the combination of the first-principles molecular dynamics (FPMD) calculations and chemical EOS models. The two multiphase EOS and SCVH models are widely applied in astrophysics [4,57]. It is clear from Fig. 2(a) that for the first two shocked states, all the theoretical models predict behavior consistent with the experimental data for densities below ∼0.16 g/cm$^3$ or pressures below ∼10 GPa. The be-
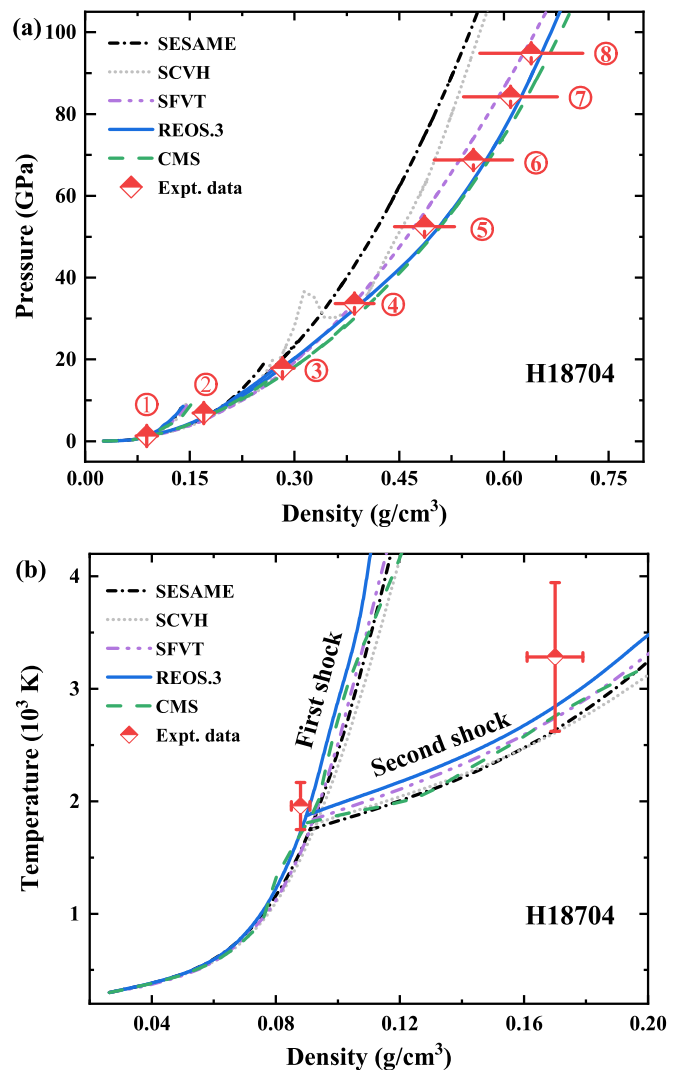


FIG. 2. (a) Pressure as a function of the density of H$_2$ for shot no. H18704 under multishock compressions. Theoretical multishock Hugoniots are shown for the SESAME model [26] (dash-dotted lines), the SCVH model [27] (dotted lines), the SFVT model [40] (dash-double-dotted lines), the REOS.3 model [33] (solid lines), and the CMS model [35] (dashed lines). Our experimental data are represented by half-filled diamonds. (b) Single- and double-shock temperature vs density for shot no. H18704. The lines and symbols are as in (a).

havior of the SESAME [26], SCVH [27], and SFVT [28] at low pressure confirm the previous experimental conclusion for H$_2$ and D$_2$ [5,11]. The trends of the REOS.3 and CMS models are similar to those of the chemical models in this region. However, with increasing pressure, the SESAME and SCVH models show a stiffer behavior and gradually deviate from the experimental data. That may be because effective pair potentials or the methods adopted in the SESAME and SCVH models cannot accurately describe the multibody interaction caused by the effects of high temperature and high pressure [33,35]. Note that in Fig. 2(a), a kink occurs on the compression curve produced by the SCVH model at the fourth shock. This implicitly indicates that the EOS surface of the SCVH model deviates from the actual system. The

data table for the REOS.3 and CMS models was constructed by a FPMD calculation using the Perdew-Burke-Ernzerhof formulation (PBE) [58] of the exchange-correlation functional in the high-pressure regime. It can be seen that these results are in good agreement with the experimental data within the error bar for the pressure above 10 GPa up to the eighth-shock compression at ∼95 GPa, even though the REOS.3 model has a slightly stiffer behavior than the CMS model, especially for pressures above 80 GPa. Moreover, we can see that the SFVT model can also give satisfactory results up to the eighth-shock compression for our experimental $P - \rho$ data.

Temperature is also a fundamental thermodynamic variable and can provide an important constraint on EOS models [59,60]. The experimental first- and second-shock temperatures of hydrogen are compared with those from theoretical models in Fig. 2(b) and Fig. S22 of the SM [54]. The measured first- and second-shock temperatures of $H_2$ are consistent with those from the theoretical models on the whole, especially REOS.3 and CMS. A comparison of the theoretical models shows that, in general, REOS.3 and SFVT predict higher and more moderate temperatures, respectively, while the temperatures predicted by SCVH and SESAME are close to each other and lower. The temperatures from CMS are basically between those of the REOS.3 and SCVH models, and have a slight bend above ∼0.08 g/cm³. This may be because, during the construction of the CMS model, there was a a large gap in the interpolation connecting the chemical model and FPMD data ($H_2$ in 0.05–0.3 g/cm³).

The multishock experiments provide principal- and off-Hugoniot states close to the conditions in giant planetary interiors. Thus, it is useful to revisit the thermodynamic space of existing experimental data. Figure 3 compares our data with the available experimental data for hydrogen. Our multishock data go beyond the pressure limit of the previous single-shock gas gun experiments [5,6] and are comparable to an intense laser shock experiment using a precompressed hydrogen sample in a diamond anvil cell (DAC) [19]. Our experiments, thus, build a bridge in thermodynamic space between the existing gas gun data in the low-pressure region and the laser data in the high-pressure region. In addition, our data reach a higher compression ratio ($\rho/\rho_0$ up to ∼43; see Table S4 of the SM [54]). The theoretical isentrope of $H_2$ for Jovian conditions (65 K and 1 bar in the atmosphere) is also shown in Fig. 3, as calculated through the following differential equation [41]:

$$\left(\frac{\partial T}{\partial \rho}\right)_s = \frac{T}{\rho^2} \frac{(\partial P/\partial T)_\rho}{(\partial E/\partial T)_\rho}, \qquad (1)$$

where $\rho$, $T$, $P$, $E$, and $S$ denote the density, temperature, pressure, specific internal energy, and entropy, respectively. The present multishock data roughly follow the calculated isentrope. In contrast, most of the laser shock data [17,19,56] are near the principal-Hugoniot curve for a liquid with an initial density of 0.076 g/cm³. However, the laser data (25–75 GPa) of Loubeyre *et al.* [19,56] for an initial state at ∼1 GPa and 297 K are comparable to the present data for the fourth- to sixth-shock states since their thermodynamic states are close in $P - \rho - T$ space. Overall, compared with the available single-shock data, our multishock data are closer to the isentrope of hydrogen in giant planetary interiors and are favorable
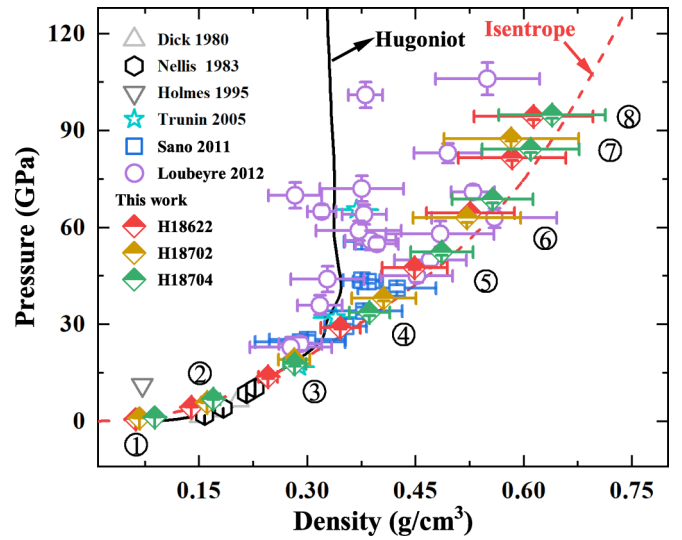


FIG. 3. Comparisons of the present data with available experimental data for hydrogen in pressure vs density plane. Our data are represented by half-filled diamonds. The numbers in circles represent the $i$th-shock state. Data from previous shock compression experiments on hydrogen using a gas gun (black hexagons [5] and gray downward triangles [6]), convergent explosives (gray upward triangles [55] and cyan stars [22]), and laser shocks (blue squares [17] and purple circles [19,56]) are also shown. The theoretical principal Hugoniot curve (solid line) and isentrope (dashed line) calculated by the REOS.3 model [33] start from the initial conditions of the laser experiment [17] and Jovian condition, respectively.

for constraining Jovian planetary models. In addition, we also use the first-principles method to calculate the conductivities and reflectivities of gaseous hydrogen along the multishock compression path to give an estimation of whether the present multishock states can reach into the metallization region; see more details of the SM [54].

Using the multishock compression technique, as well as obtaining the EOS data for gaseous $H_2$ up to 95 GPa, we also achieved a dynamic loading from shock adiabatic to quasi-isentropic compression [48]. The compression process can be analyzed by the variations of the calculated specific entropy along the multishock compression path, as shown in Fig. S23 of the SM [54]. The result shows that the entropy hardly changes after the fifth shock. Therefore, the multishock compression starting at the fifth shock can be regarded as quasi-isentropic, enabling us to infer the isentropic sound velocity ($C_s$). Note that the $C_s$ of only two shots, no. H18622 and no. H18704, can be derived from the nature of the quasi-isentropic compression. A detailed derivation can be found in Sec. VII of the SM [54].

Measurements of the sound velocity of high-pressure hydrogen can not only provide a different perspective to validate the theoretical models, but also play a vital role in connecting the theoretical Jovian model to seismic observations of Jupiter, which is an important input parameter to determine the characteristic frequency $\nu_0$ of Jovian oscillation from the theoretical Jovian model [63,65]. A comparison of measured $C_s$ and those predicted by the theoretical modes shows that some chemical models become inapplicable in the high-
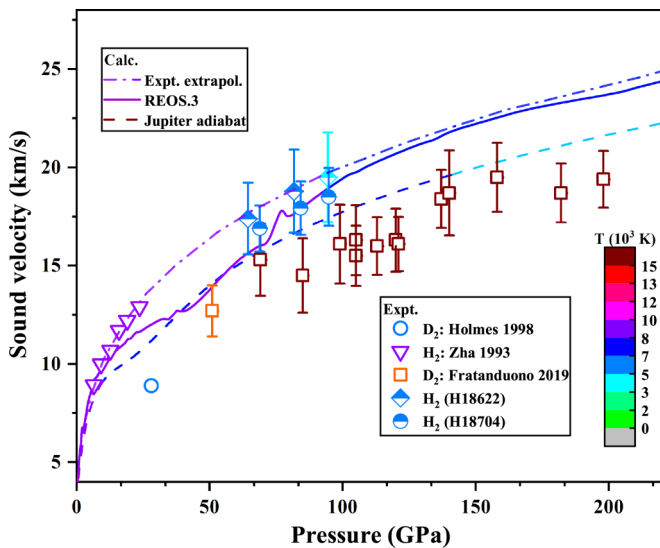
FIG. 4. Sound velocities of hydrogen (deuterium) vs pressure. Half-filled diamonds and circles correspond to the sound velocities of shots no. H18622 and no. H18704, respectively. The previous experimental data are from Holmes *et al.* (open circles) [61], Zha *et al.* (open triangles) [46], and Fratanduono *et al.* (open squares) [62]. The pure hydrogen isentropes for the Jovian conditions include the calculated result by the REOS.3 model (solid line) and extrapolated experimental results (dash-dotted line) by Duffy *et al.* [63]. A Jupiter adiabat (dashed line) based on the hydrogen-helium-water mixtures EOSs [64] is also shown. The temperature of all data points and curves is indicated by the color bar.

pressure region, especially for the SCVH model; see Sec. VII of the SM [54]. We note that the observed $v_0$ are consistent with the theoretical Jovian models and $C_s$ extrapolated by Duffy *et al.* [63], which were measured by Zha *et al.* [46] at room temperature in a DAC using Brillouin scattering technology and limited to a lower pressure. Our measured $C_s$ above 60 GPa agrees well with the extrapolated results; see Fig. 4. The present $C_s$ values of $H_2$ are also compared with available experimental results for $H_2$ [46] and $D_2$ [61,62] in Fig. 4. Our data significantly expand the measured ranges of temperature and pressure for the $C_s$ value of hydrogen, compared to prior $C_s$ values measured by Zha *et al.* [46]. As for deuterium, experimental $C_s$ data were derived from light-gas gun experiments using a shock-overtake technique [61] or laser experiments using an unsteady-wave technique [62]. The value of $C_s$ for hydrogen from our experiments is higher than that for deuterium from the laser experiments at the same pressure, even though deuterium has a higher temperature (above 15.0 kK) along the principal-Hugoniot curve. The hydrogen isentrope for the Jovian conditions shows a slightly

higher sound velocity and lower temperature than the Jupiter adiabat [64], for which the contributions from other components, such as He and $H_2O$, are also considered. Note that $C_s$ for hydrogen is closer to the Jupiter adiabat than that for the data in the laser experiments [62] because the quasi-isentropic compression provides a relatively slow temperature rise. In addition, the accurately measured Jupiter's gravitational field from the Juno mission [66–69] has been used to constrain Jupiter's interior structure models [3,70], which are derived from the EOS, assumed type of temperature profile (adiabatic or not), and a temperature boundary condition at the observed atmosphere [71]. Our obtained EOS and sound velocity data are closer to the thermodynamic states in Jupiter's interiors compared to the prior experimental data, and can provide more experimental constraints to theoretical EOS models used to construct Jupiter's interior structure models based on Juno's gravity data.

## IV. CONCLUSIONS

In summary, EOS and sound velocity measurements for dense gaseous $H_2$ have been obtained through compression experiments. The pressure and density were determined up to 95 GPa and 0.64 g/cm$^3$, respectively. Various theoretical models have been revisited using the present EOS data. The comparison between our experimental results and theoretical models shows that the chemical models SESAME, SCVH, and SFVT, and multiphase EOS models REOS.3 and CMS, all can give satisfactory results in a low-pressure region. In a high-pressure region, the SFVT, REOS.3, and CMS models are still consistent with the experimental EOS; however, the SESAME and SCVH models exhibit obvious stiffer behaviors. Our EOS data support using the REOS.3 and CMS models to construct interior models for Jupiter. And the $C_s$ derived from the multishock states and EOS data are closer to Jupiter's interior conditions than previous $C_s$ measurements for hydrogen and deuterium, which are more suitable for constraining and developing interior structure models of Jupiter over a wider pressure and temperature region.

[1] A. Alavi, M. Parrinello, and D. Frenkel, *Ab initio* calculation of the sound velocity of dense hydrogen: Implications for models of Jupiter, Science **269**, 1252 (1995).

[2] J. M. McMahon, M. A. Morales, C. Pierleoni, and D. M. Ceperley, The properties of hydrogen and helium under extreme conditions, Rev. Mod. Phys. **84**, 1607 (2012).

[3] F. Debras and G. Chabrier, New models of Jupiter in the context of Juno and Galileo, Astrophys. J. **872**, 100 (2019).

[4] R. Helled, G. Mazzola, and R. Redmer, Understanding dense hydrogen at planetary conditions, Nat. Rev. Phys. **2**, 562 (2020).

[5] W. J. Nellis, A. C. Mitchell, M. van Thiel, G. J. Devine, R. J. Trainor, and N. Brown, Equation-of-state data for molecular

hydrogen and deuterium at shock pressures in the range 2–76 GPa (20–760 kbar), J. Chem. Phys. **79**, 1480 (1983).

[6] N. C. Holmes, M. Ross, and W. J. Nellis, Temperature measurements and dissociation of shock-compressed liquid deuterium and hydrogen, Phys. Rev. B **52**, 15835 (1995).

[7] S. T. Weir, A. C. Mitchell, and W. J. Nellis, Metallization of Fluid Molecular Hydrogen at 140 GPa (1.4 Mbar), Phys. Rev. Lett. **76**, 1860 (1996).

[8] W. J. Nellis, S. T. Weir, and A. C. Mitchell, Minimum metallic conductivity of fluid hydrogen at 140 GPa (1.4 Mbar), Phys. Rev. B **59**, 3434 (1999).

[9] M. D. Knudson, D. L. Hanson, J. E. Bailey, C. A. Hall, J. R. Asay, and W. W. Anderson, Equation of State Measurements in Liquid Deuterium to 70 GPa, Phys. Rev. Lett. **87**, 225501 (2001).

[10] M. D. Knudson, D. L. Hanson, J. E. Bailey, C. A. Hall, and J. R. Asay, Use of a Wave Reverberation Technique to Infer the Density Compression of Shocked Liquid Deuterium to 75 GPa, Phys. Rev. Lett. **90**, 035505 (2003).

[11] M. D. Knudson, D. L. Hanson, J. E. Bailey, C. A. Hall, J. R. Asay, and C. Deeney, Principal Hugoniot, reverberating wave, and mechanical reshock measurements of liquid deuterium to 400 GPa using plate impact techniques, Phys. Rev. B **69**, 144209 (2004).

[12] M. D. Knudson and M. P. Desjarlais, High-Precision Shock Wave Measurements of Deuterium: Evaluation of Exchange-Correlation Functionals at the Molecular-to-Atomic Transition, Phys. Rev. Lett. **118**, 035501 (2017).

[13] L. B. Da Silva, P. Celliers, G. W. Collins, K. S. Budil, N. C. Holmes, T. W. Barbee Jr., B. A. Hammel, J. D. Kilkenny, R. J. Wallace, M. Ross, R. Cauble, A. Ng, and G. Chiu, Absolute Equation of State Measurements on Shocked Liquid Deuterium up to 200 GPa (2 Mbar), Phys. Rev. Lett. **78**, 483 (1997).

[14] P. M. Celliers, G. W. Collins, L. B. Da Silva, D. M. Gold, R. Cauble, R. J. Wallace, M. E. Foord, and B. A. Hammel, Shock-Induced Transformation of Liquid Deuterium into a Metallic Fluid, Phys. Rev. Lett. **84**, 5564 (2000).

[15] A. N. Mostovych, Y. Chan, T. Lehecha, A. Schmitt, and J. D. Sethian, Reflected Shock Experiments on the Equation-of-State Properties of Liquid Deuterium at 100–600 GPa (1–6 Mbar), Phys. Rev. Lett. **85**, 3870 (2000).

[16] D. G. Hicks, T. R. Boehly, P. M. Celliers, J. H. Eggert, S. J. Moon, D. D. Meyerhofer, and G. W. Collins, Laser-driven single shock compression of fluid deuterium from 45 to 220 GPa, Phys. Rev. B **79**, 014112 (2009).

[17] T. Sano, N. Ozaki, T. Sakaiya, K. Shigemori, M. Ikoma, T. Kimura, K. Miyanishi, T. Endo, A. Shiroshita, H. Takahashi, T. Jitsui, Y. Hori, Y. Hironaka, A. Iwamoto, T. Kadono, M. Nakai, T. Okuchi, K. Otani, K. Shimizu, T. Kondo *et al.*, Laser-shock compression and Hugoniot measurements of liquid hydrogen to 55 GPa, Phys. Rev. B **83**, 054117 (2011).

[18] K. Falk, S. P. Regan, J. Vorberger, M. A. Barrios, T. R. Boehly, D. E. Fratanduono, S. H. Glenzer, D. G. Hicks, S. X. Hu, C. D. Murphy, P. B. Radha, S. Rothman, A. P. Jephcoat, J. S. Wark, D. O. Gericke, and G. Gregori, Self-consistent measurement of the equation of state of liquid deuterium, High Energy Density Phys. **8**, 76 (2012).

[19] P. Loubeyre, S. Brygoo, J. Eggert, P. M. Celliers, D. K. Spaulding, J. R. Rygg, T. R. Boehly, G. W. Collins, and R. Jeanloz, Extended data set for the equation of state of warm dense hydrogen isotopes, Phys. Rev. B **86**, 144115 (2012).

[20] A. Fernandez-Pañella, M. Millot, D. E. Fratanduono, M. P. Desjarlais, S. Hamel, M. C. Marshall, D. J. Erskine, P. A. Sterne, S. Haan, T. R. Boehly, G. W. Collins, J. H. Eggert, and P. M. Celliers, Shock Compression of Liquid Deuterium up to 1 TPa, Phys. Rev. Lett. **122**, 255702 (2019).

[21] G. V. Boriskov, A. I. Bykov, R. I. Iľkaev, V. D. Selemir, G. V. Simakov, R. F. Trunin, V. D. Urlin, A. N. Shuikin, and W. J. Nellis, Shock compression of liquid deuterium up to 109 GPa, Phys. Rev. B **71**, 092104 (2005).

[22] R. F. Trunin, G. V. Boriskov, S. I. Belov, A. I. Bykov, R. I. Iľkaev, G. V. Simakov, V. D. Urlin, and A. N. Shuikin, Shock-wave compression of hydrogen to pressures of 65 GPa, JETP Lett. **82**, 284 (2005).

[23] V. E. Fortov, R. I. Ilkaev, V. A. Arinin, V. V. Burtzev, V. A. Golubev, I. L. Iosilevskiy, V. V. Khrustalev, A. L. Mikhailov, M. A. Mochalov, V. Y. Ternovoi, and M. V. Zhernokletov, Phase Transition in a Strongly Nonideal Deuterium Plasma Generated by Quasi-Isentropical Compression at Megabar Pressures, Phys. Rev. Lett. **99**, 185001 (2007).

[24] M. A. Mochalov, R. I. Iľkaev, V. E. Fortov, A. L. Mikhailov, A. O. Blikov, V. A. Ogorodnikov, V. K. Gryaznov, and I. L. Iosilevskii, Quasi-isentropic compressibility of a strongly non-ideal deuterium plasma at pressures of up to 5500 GPa: Nonideality and degeneracy effects, J. Expt. Theor. Phys. **124**, 505 (2017).

[25] M. A. Mochalov, R. I. Iľkaev, V. E. Fortov, A. L. Mikhailov, V. A. Arinin, A. O. Blikov, V. A. Komrakov, I. P. Maksimkin, V. A. Ogorodnikov, and A. V. Ryzhkov, Quasi-isentropic compressibility of deuterium at a pressure of ~12 TPa, JETP Lett. **107**, 168 (2018).

[26] G. I. Kerley, Equation of state and phase diagram of dense hydrogen, Phys. Earth Planet. Inter. **6**, 78 (1972).

[27] D. Saumon, G. Chabrier, and H. M. van Horn, An equation of state for low-mass stars and giant planets, Astrophys. J. Suppl. Ser. **99**, 713 (1995).

[28] Q. Chen, L. Cai, Y. Zhang, Y. Gu, and F. Jing, Self-consistent fluid variational theory for the equation of state and dissociation of dense hydrogen and nitrogen, J. Phys.: Condens. Matter **19**, 425209 (2007).

[29] T. J. Lenosky, J. D. Kress, L. A. Collins, and I. Kwon, Molecular-dynamics modeling of shock-compressed liquid hydrogen, Phys. Rev. B **55**, R11907 (1997).

[30] B. Militzer and D. M. Ceperley, Path Integral Monte Carlo Calculation of the Deuterium Hugoniot, Phys. Rev. Lett. **85**, 1890 (2000).

[31] M. P. Desjarlais, Density-functional calculations of the liquid deuterium Hugoniot, reshock, and reverberation timing, Phys. Rev. B **68**, 064204 (2003).

[32] L. Caillabet, S. Mazevet, and P. Loubeyre, Multiphase equation of state of hydrogen from *ab initio* calculations in the range 0.2 to 5 g/cc up to 10 eV, Phys. Rev. B **83**, 094101 (2011).

[33] A. Becker, W. Lorenzen, J. J. Fortney, N. Nettelmann, M. Schöttler, and R. Redmer, *Ab initio* equations of state for hydrogen (H-REOS.3) and helium (He-REOS.3) and their implications for the interior of brown dwarfs, Astrophys. J. Suppl. Ser. **215**, 21 (2014).

[34] N. M. Tubman, E. Liberatore, C. Pierleoni, M. Holzmann, and D. M. Ceperley, Molecular-Atomic Transition along the Deuterium Hugoniot Curve with Coupled Electron-Ion Monte Carlo Simulations, Phys. Rev. Lett. **115**, 045301 (2015).

[35] G. Chabrier, S. Mazevet, and F. Soubiran, A new equation of state for dense hydrogen-helium mixtures, Astrophys. J. **872**, 51 (2019).

[36] M. D. Knudson, M. P. Desjarlais, A. Becker, R. W. Lemke, K. R. Cochrane, M. E. Savage, D. E. Bliss, T. R. Mattsson, and R. Redmer, Direct observation of an abrupt insulator-to-metal transition in dense liquid deuterium, Science **348**, 1455 (2015).

[37] P. M. Celliers, M. Millot, S. Brygoo, R. S. McWilliams, D. E. Fratanduono, J. R. Rygg, A. F. Goncharov, P. Loubeyre, J. H. Eggert, J. L. Peterson, N. B. Meezan, S. Le Pape, G. W. Collins, R. Jeanloz, and R. J. Hemley, Insulator-metal transition in dense fluid deuterium, Science **361**, 677 (2018).

[38] W. Ebeling and W. Richert, Plasma phase transition in hydrogen, Phys. Lett. A **108**, 80 (1985).

[39] D. Saumon and G. Chabrier, Fluid hydrogen at high density: Pressure ionization, Phys. Rev. A **46**, 2084 (1992).

[40] A. V. Chentsov and P. R. Levashov, Isentropic compression of deuterium by quantum molecular dynamics, Contrib. Plasma Phys. **52**, 33 (2012).

[41] A. Becker, N. Nettelmann, B. Holst, and R. Redmer, Isentropic compression of hydrogen: Probing conditions deep in planetary interiors, Phys. Rev. B **88**, 045122 (2013).

[42] H. Y. Geng, Q. Wu, M. Marqués, and G. J. Ackland, Thermodynamic anomalies and three distinct liquid-liquid transitions in warm dense liquid hydrogen, Phys. Rev. B **100**, 134109 (2019).

[43] P. M. Celliers, M. Millot, S. Brygoo, R. S. McWilliams, D. E. Fratanduono, J. R. Rygg, A. F. Goncharov, P. Loubeyre, J. H. Eggert, J. L. Peterson, N. B. Meezan, S. Le Pape, G. W. Collins, R. Jeanloz, and R. J. Hemley, Response to Comment on "Insulator-metal transition in dense fluid deuterium", Science **363**, eaaw1970 (2019).

[44] M. P. Desjarlais, M. D. Knudson, and R. Redmer, Comment on "Insulator-metal transition in dense fluid deuterium", Science **363**, eaaw0969 (2019).

[45] M. P. Desjarlais, M. D. Knudson, and R. Redmer, Thermodynamics of the insulator-metal transition in dense liquid deuterium, Phys. Rev. B **101**, 104101 (2020).

[46] C.-s. Zha, T. S. Duffy, H.-k. Mao, and R. J. Hemley, Elasticity of hydrogen to 24 GPa from single-crystal Brillouin scattering and synchrotron x-ray diffraction, Phys. Rev. B **48**, 9246 (1993).

[47] J. Zheng, Q. F. Chen, Y. J. Gu, J. T. Li, Z. G. Li, C. J. Li, and Z. Y. Chen, Shock-adiabatic to quasi-isentropic compression of warm dense helium up to 150 GPa, Phys. Rev. B **95**, 224104 (2017).

[48] G.-J. Li, Z.-G. Li, Q.-F. Chen, Y.-J. Gu, W. Zhang, L. Liu, H.-Y. Geng, Z.-Q. Wang, Y.-S. Lan, Y. Hou, J.-Y. Dai, and X.-R. Chen, Multishock to Quasi-Isentropic Compression of Dense Gaseous Deuterium-Helium Mixtures up to 120 GPa: Probing the Sound Velocities Relevant to Planetary Interiors, Phys. Rev. Lett. **126**, 075701 (2021).

[49] N. C. Holmes, Fiber-coupled optical pyrometer for shock-wave studies, Rev. Sci. Instrum. **66**, 2615 (1995).

[50] T. Tao, X. Wang, H. Ma, S. Liu, X. Li, and J. Weng, Note: Using an optical phase-locked loop in heterodyne velocimetry, Rev. Sci. Instrum. **84**, 076101 (2013).

[51] Z.-G. Li, Q.-F. Chen, Y.-J. Gu, J. Zheng, and X.-R. Chen, Measurements of the principal Hugoniots of dense gaseous deuterium-helium mixtures: Combined multichannel optical pyrometry, velocity interferometry, and streak optical pyrometry measurements, AIP Adv. **6**, 105309 (2016).

[52] Z.-G. Li, Q.-F. Chen, Y.-J. Gu, J. Zheng, W. Zhang, L. Liu, G.-J. Li, Z.-Q. Wang, and J.-Y. Dai, Multishock compression of dense cryogenic hydrogen-helium mixtures up to 60 GPa: Validating the equation of state calculated from first principles, Phys. Rev. B **98**, 064101 (2018).

[53] L. Liu, Q.-F. Chen, Y.-J. Gu, W. Zhang, Z.-G. Li, C.-J. Li, Z.-Q. Wang, G.-J. Li, Y.-S. Lan, and X.-R. Chen, Measurement of multiple physical parameters of dense gaseous hydrogen-deuterium mixture under double-shock compression: Evaluating theoretical models from multiple views, Appl. Phys. Lett. **115**, 231905 (2019).

[54] See Supplemental Material at http://link.aps.org/supplemental/10.1103/PhysRevB.107.014309 for the analysis and summary of the experimental data, the theoretical calculation, and supplemental Figs. S1–S30 and Tables S1–S4, which include Refs. [3,7,8,14,19,26–28,33,35,37,47–49,53,56,58,72–105].

[55] R. D. Dick and G. I. Kerley, Shock compression data for liquids. II. Condensed hydrogen and deuterium, J. Chem. Phys. **73**, 5264 (1980).

[56] S. Brygoo, M. Millot, P. Loubeyre, A. E. Lazicki, S. Hamel, T. Qi, P. M. Celliers, F. Coppari, J. H. Eggert, D. E. Fratanduono, D. G. Hicks, J. R. Rygg, R. F. Smith, D. C. Swift, G. W. Collins, and R. Jeanloz, Analysis of laser shock experiments on precompressed samples using a quartz reference and application to warm dense hydrogen and helium, J. Appl. Phys. **118**, 195901 (2015).

[57] G. Chabrier and F. Debras, A new equation of state for dense hydrogen-helium mixtures. II. Taking into account hydrogen-helium interactions, Astrophys. J. **917**, 4 (2021).

[58] J. P. Perdew, K. Burke, and M. Ernzerhof, Generalized Gradient Approximation Made Simple, Phys. Rev. Lett. **77**, 3865 (1996).

[59] W. J. Nellis, M. Ross, and N. C. Holmes, Temperature-measurements of shock-compressed liquid hydrogen: Implications for the interior of Jupiter, Science **269**, 1249 (1995).

[60] G. W. Collins, P. M. Celliers, L. B. Da Silva, R. Cauble, D. M. Gold, M. E. Foord, N. C. Holmes, B. A. Hammel, R. J. Wallace, and A. Ng, Temperature Measurements of Shock Compressed Liquid Deuterium up to 230 GPa, Phys. Rev. Lett. **87**, 165504 (2001).

[61] N. C. Holmes, W. J. Nellis, and M. Ross, Sound velocities in shocked liquid deuterium, AIP Conf. Proc. **429**, 61 (1998).

[62] D. E. Fratanduono, M. Millot, A. Fernandez Pañella, P. A. Sterne, G. W. Collins, D. G. Hicks, J. H. Eggert, T. R. Boehly, and P. M. Celliers, Measurement of the sound speed in dense fluid deuterium along the cryogenic liquid Hugoniot, Phys. Plasmas **26**, 012710 (2019).

[63] T. S. Duffy, W. L. Vos, C. S. Zha, R. J. Hemley, and H. K. Mao, Sound velocities in dense hydrogen and the interior of Jupiter, Science **263**, 1590 (1994).

[64] M. French, A. Becker, W. Lorenzen, N. Nettelmann, M. Bethkenhagen, J. Wicht, and R. Redmer, *Ab initio* simulations for material properties along the Jupiter adiabat, Astrophys. J. Suppl. Ser. **202**, 5 (2012).

[65] N. Nettelmann, A. Becker, B. Holst, and R. Redmer, Jupiter models with improved *ab initio* hydrogen equation of state (H-Reos.2), Astrophys. J. **750**, 52 (2012).

[66] S. J. Bolton, A. Adriani, V. Adumitroaie, M. Allison, J. Anderson, S. Atreya, J. Bloxham, S. Brown, J. E. P. Connerney, E. DeJong, W. Folkner, D. Gautier, D. Grassi, S. Gulkis, T. Guillot, C. Hansen, W. B. Hubbard, L. Iess, A. Ingersoll, M. Janssen *et al.*, Jupiter's interior and deep atmosphere: The initial pole-to-pole passes with the Juno spacecraft, Science **356**, 821 (2017).

[67] W. M. Folkner, L. Iess, J. D. Anderson, S. W. Asmar, D. R. Buccino, D. Durante, M. Feldman, L. Gomez Casajus, M. Gregnanin, A. Milani, M. Parisi, R. S. Park, D. Serra, G. Tommei, P. Tortora, M. Zannoni, S. J. Bolton, J. E. P. Connerney, and S. M. Levin, Jupiter gravity field estimated from the first two Juno orbits, Geophys. Res. Lett. **44**, 4694 (2017).

[68] D. Durante, M. Parisi, D. Serra, M. Zannoni, V. Notaro, P. Racioppa, D. R. Buccino, G. Lari, L. Gomez Casajus, L. Iess, W. M. Folkner, G. Tommei, P. Tortora, and S. J. Bolton, Jupiter's gravity field halfway through the Juno mission, Geophys. Res. Lett. **47**, e2019GL086572 (2020).

[69] D. Durante, T. Guillot, L. Iess, D. J. Stevenson, C. R. Mankovich, S. Markham, E. Galanti, Y. Kaspi, M. Zannoni, L. Gomez Casajus, G. Lari, M. Parisi, D. R. Buccino, R. S. Park, and S. J. Bolton, Juno spacecraft gravity measurements provide evidence for normal modes of Jupiter, Nat. Commun. **13**, 4632 (2022).

[70] S. M. Wahl, W. B. Hubbard, B. Militzer, T. Guillot, Y. Miguel, N. Movshovitz, Y. Kaspi, R. Helled, D. Reese, E. Galanti, S. Levin, J. E. Connerney, and S. J. Bolton, Comparing Jupiter interior structure models to Juno gravity measurements and the role of a dilute core, Geophys. Res. Lett. **44**, 4649 (2017).

[71] R. Helled, D. J. Stevenson, J. I. Lunine, S. J. Bolton, N. Nettelmann, S. Atreya, T. Guillot, B. Militzer, Y. Miguel, and W. B. Hubbard, Revelations on Jupiter's formation, evolution and interior: Challenges from Juno results, Icarus **378**, 114937 (2022).

[72] Y. J. Gu, Q. F. Chen, J. Zheng, L. C. Cai, O. H. Jia, Z. Y. Chen, and F. Q. Jing, The equation of state, shock-induced molecule dissociation, and transparency loss for multi-compressed dense gaseous $H_2 + D_2$ mixtures, J. Appl. Phys. **111**, 013513 (2012).

[73] A. M. Brandis and B. A. Cruden, Shock tube radiation measurements in nitrogen, in *2018 Joint Thermophysics and Heat Transfer Conference*, AIAA Aviation Forum (American Institute of Aeronautics and Astronautics, Reston, Virginia, 2018).

[74] W. J. Nellis, A. C. Mitchell, and D. A. Young, Equation-of-state measurements for aluminum, copper, and tantalum in the pressure range 80–440 GPa (0.8–4.4 Mbar), J. Appl. Phys. **93**, 304 (2003).

[75] J. M. Brown and R. G. McQueen, Phase transitions, Grüneisen parameter, and elasticity for shocked iron between 77 GPa and 400 GPa, J. Geophys. Res. **91**, 7485 (1986).

[76] R. G. McQueen, Shock waves in condensed media: Their properties and the equations of state of materials derived from them, Report No. LA-UR-90-1996 (Los Alamos National Laboratory, Los Alamos, NM, 1989).

[77] W. J. Nellis, Dynamic compression of materials: Metallization of fluid hydrogen at high pressures, Rep. Prog. Phys. **69**, 1479 (2006).

[78] Q. Chen, L. Cai, D. Chen, and F. Jing, The equation of state for the mixtures of dense hydrogen and deuterium, Phys. B: Condens. Matter **348**, 299 (2004).

[79] Y. J. Gu, Q. F. Chen, L. C. Cai, Z. Y. Chen, J. Zheng, and F. Q. Jing, Multishock comparison of dense gaseous $H_2$+He mixtures up to 30 GPa, J. Chem. Phys. **130**, 184506 (2009).

[80] W. X. Li, *One-dimensional Nonsteady Flow and Shock Waves* (National Defense Industry Press, Beijing, 2003).

[81] H. Tan, *Experimental Shock Wave Physics* (National Defense Industry Press, Beijing, 2018).

[82] T. S. Duffy and T. J. Ahrens, Dynamic compression of an Fe-Cr-Ni alloy to 80 GPa, J. Appl. Phys. **82**, 4259 (1997).

[83] J. Weng, T. Tao, S. Liu, H. Ma, X. Wang, C. Liu, and H. Tan, Optical-fiber frequency domain interferometer with nanometer resolution and centimeter measuring range, Rev. Sci. Instrum. **84**, 113103 (2013).

[84] C. T. Seagle, J.-P. Davis, and M. D. Knudson, Mechanical response of lithium fluoride under off-principal dynamic shock-ramp loading, J. Appl. Phys. **120**, 165902 (2016).

[85] W. Wang, H. Chen, and X. Wang, Compact all fiber interior ballistic projectile velocity measurement system, J. Appl. Opt. **32**, 723 (2011).

[86] J. Weng, H. Tan, X. Wang, Y. Ma, S. Hu, and X. Wang, Optical-fiber interferometer for velocity measurements with picosecond resolution, Appl. Phys. Lett. **89**, 111101 (2006).

[87] S. P. Marsh, *LASL Shock Hugoniot Data* (University of California Press, Berkeley, 1980).

[88] L. Hao, X. Wang, Q.-S. Wang, Q. Kang, and J. Huang, Dynamic response and optical properties of *pmma* under shock compression, Chin. J. High Pressure Phys. **31**, 579 (2017).

[89] N. Winfree, L. Chhabildas, W. Reinhart, D. Carroll, and G. Kerley, EOS data of Ti-6Al-4V to impact velocities of 10.4 km/s on a three-stage gun, AIP Conf. Proc. **620**, 75 (2002).

[90] J. Tang, Y. J. Gu, Q. F. Chen, Z. G. Li, J. Zheng, C. J. Li, and J. T. Li, Multiple shock reverberation compression of dense Ne up to the warm dense regime: Evaluating the theoretical models, Phys. Rev. B **97**, 140101(R) (2018).

[91] G. Kresse and J. Furthmüller, Efficient iterative schemes for *ab initio* total-energy calculations using a plane-wave basis set, Phys. Rev. B **54**, 11169 (1996).

[92] M. Dion, H. Rydberg, E. Schröder, D. C. Langreth, and B. I. Lundqvist, Van der Waals Density Functional for General Geometries, Phys. Rev. Lett. **92**, 246401 (2004).

[93] P. E. Blöchl, Projector augmented-wave method, Phys. Rev. B **50**, 17953 (1994).

[94] G. Kresse and D. Joubert, From ultrasoft pseudopotentials to the projector augmented-wave method, Phys. Rev. B **59**, 1758 (1999).

[95] A. Baldereschi, Mean-value point in the Brillouin zone, Phys. Rev. B **7**, 5212 (1973).

[96] S. Nosé, A unified formulation of the constant temperature molecular dynamics methods, J. Chem. Phys. **81**, 511 (1984).

[97] W. G. Hoover, Canonical dynamics: Equilibrium phase-space distributions, Phys. Rev. A **31**, 1695 (1985).

[98] R. Kubo, Statistical-mechanical theory of irreversible processes. I. General theory and simple applications to magnetic and conduction problems, J. Phys. Soc. Jpn. **12**, 570 (1957).

[99] D. A. Greenwood, The Boltzmann equation in the theory of electrical conduction in metals, Proc. Phys. Soc. **71**, 585 (1958).

[100] L. Calderín, V. V. Karasiev, and S. B. Trickey, Kubo-Greenwood electrical conductivity formulation and implementation for projector augmented wave datasets, Comput. Phys. Commun. **221**, 118 (2017).

[101] P. Giannozzi Jr., O. Andreussi, T. Brumme, O. Bunau, M. Buongiorno Nardelli, M. Calandra, R. Car, C. Cavazzoni, D. Ceresoli, M. Cococcioni, N. Colonna, I. Carnimeo, A. Dal Corso, S. de Gironcoli, P. Delugas, R. A. DiStasio, A. Ferretti, A. Floris, G. Fratesi, G. Fugallo *et al.*, Advanced capabilities for materials modelling with QUANTUM ESPRESSO, J. Phys.: Condens. Matter **29**, 465901 (2017).

[102] H. J. Monkhorst and J. D. Pack, Special points for Brillouin-zone integrations, Phys. Rev. B **13**, 5188 (1976).

[103] S. Jiang, N. Holtgrewe, Z. M. Geballe, S. S. Lobanov, M. F. Mahmood, R. S. McWilliams, and A. F. Goncharov, A spectroscopic study of the insulator-metal transition in liquid hydrogen and deuterium, Adv. Sci. **7**, 1901668 (2020).

[104] M. D. Knudson, M. P. Desjarlais, M. Preising, and R. Redmer, Evaluation of exchange-correlation functionals with multiple-shock conductivity measurements in hydrogen and deuterium at the molecular-to-atomic transition, Phys. Rev. B **98**, 174110 (2018).

[105] G. Rillo, M. A. Morales, D. M. Ceperley, and C. Pierleoni, Optical properties of high-pressure fluid hydrogen across molecular dissociation, Proc. Natl. Acad. Sci. USA **116**, 9770 (2019).